Journal of The Electrochemical Society, 2022 **169** 056522
1945-7111/2022/169(5)/056522/9/$40.00 © 2022 The Electrochemical Society ("ECS"). Published on behalf of ECS by IOP Publishing Limited

Photoelectrochemical Oxygen Evolution on Mesoporous Hematite Films Prepared from Maghemite Nanoparticles

N. C. Verissimo,[1,2,z] D. Ren,[1] C. C. C. Kleiner,[2] F. A. B. Hesse,[2] S. M. Zakeeruddin,[1] M. Grätzel,[1,z] and R. Bertazzoli[2]

[1]*Laboratory of Photonics and Interface—LPI Institute of Sciences and Chemical Engineering—ISIC École Polytechnique Fédérale de Lausanne, EPFL, Lausanne 1015, Switzerland*
[2]*Department of Manufacturing and Materials Engineering – DEMM University of Campinas, UNICAMP, Campinas 13083-860, São Paulo, Brazil*

Iron oxides, especially hematite (α-Fe_2O_3), are promising materials for applications in photoelectrochemical cells and photo-redox catalysis. However, realizing high-performance hematite photoanodes via an environmentally-friendly route remains a great challenge. In this work, we employed a novel approach to prepare mesoscopic hematite photoelectrodes with remarkable performance for water oxidation. Hydrothermally-synthesized maghemite nanoparticles of high crystallinity with a mean particle size of 3.3 nm were deposited onto fluorine doped tin oxide (FTO) transparent conducting glass substrates, followed by heat treatment to convert them into a homogeneous mesoporous hematite layer. A hematite photoanode with a thickness of 220 nm, delivered a maximum photocurrent density of 1.8 mA cm^{-2} for water oxidation to oxygen at 1.23 V_{RHE} under simulated AM 1.5 irradiation. Upon treating the surface of the hematite photoelectrode with Co(II) cations the photocurrent density nearly doubled at the same potential to 3.32 mA cm^{-2} placing our new photoelectrode among the best hematite-based photocatalysts for visible light induced water splitting. Further photoelectrochemical analysis provided insights into the factors boosting the performance of the hematite photoanode.
 [DOI: 10.1149/1945-7111/ac70fd]

Manuscript received April 18, 2022. Published May 26, 2022. *This paper is part of the JES Focus Issue on Focus Issue In Honor of John Goodenough: A Centenarian Milestone.*

Supplementary material for this article is available online

Nanostructured hematite stands out as the one of the most promising semiconductor materials for photoanodes due to its abundance, stability, and environmental compatibility. The bandgap of hematite lies between 1.9 to 2.2 eV, allowing it to reach up to 17% solar-to-hydrogen conversion efficiency with a maximum photocurrent of 14 mA cm^{-2}.[1–8] However, the onset potential and the photocurrent of current hematite-based photoanodes are still far from satisfying, mainly due to a short hole diffusion length (2–4 nm) and a low absorption coefficient, leading to extensive charge recombination.[3,5,9,10] Although hematite doping[11–16] and the design of new mesoscopic morphologies are widely used to improve photocurrent response,[2,4,5,7,8,17–23] a breakthrough in the development of pure hematite photoanodes from more friendly synthesis routes is urgently needed.[24,25] Although several methods have been reported for hematite synthesis in the past years, it remains a challenge to develop a facile and inexpensive methodology[26] to control the morphology and particle size. Among these methods, hydrothermal synthesis stands out as a low-cost and simple technique enabling the fabrication of different kinds of nanoparticulate morphologies by varying the parameters such as temperature, time, solvents, stabilisers, and precursors.[27]

Extensive efforts have been devoted by researchers to the hydrothermal synthesis of bare hematite photoanodes. Hematite nanorods were submitted to the evaluation of their photocurrent responses by using a range of pH values. It was found that increasing the electrolyte pH from 7.0 to 13.6 augmented the photocurrent at 1.23 V_{RHE} from 0.15 to 1.13 mA cm^2.[28] The photoanodes were synthesised by an immersion technique, where the FTO glass was placed into a 0.15 M $FeCl_3$ solution at 100 °C for 3 h, then heat-treated at 800 °C for 15 min to convert the nanowires into hematite nanorods. Using a similar approach, but with different thermal treatments (550 °C for 1 h and 800 °C for 20 min), Kim et al. produced a bare-hematite wormlike photoanode with a photocurrent of 1.26 mA cm^2 at 1.23 V_{RHE}.[3] Gonçalves et al. achieved a photocurrent of 1.4 mA cm^2 at 1.23 V_{RHE} with a mesoporous hematite produced by solvothermal technique, followed by heat-treatment at 800 °C for 20 min under a magnetic field.[6] However, the photocurrent density achieved on bare hematite photoanodes prepared via hydrothermal synthesis is still far below the theoretical limit.

In this work, we present a hydrothermal synthesis of maghemite quantum dots with controllable particle size and crystallinity, excellent stability in water, and perfect dispersity in an aqueous stabiliser solution. Heat treatment of the colloidal maghemite solution deposited onto an FTO glass substrate led to a homogeneous mesoporous hematite film. We found that its thickness, roughness and the heat-treatment strongly affected the performance of the photoanode for solar water splitting. The nanocrystalline hematite films presented in our work delivered the highest photocurrent response observed so far for bare-hematite photoanodes.

Further analysis showed that the high photocurrent may be attributed to the preferred orientation of the crystallites along the [110] and [104] axis along with effective passivation of surface defects as well as the high level of *n*-doping via oxygen vacancy formation under the high temperature heat-treatment. Nonetheless, we find that treatment of the hematite film with an aqueous Co(II) solution results in a further large increase of the photocurrent and substantial shift of its onset to lower potentials. Apparently the specific meso-porous morphology of our hematite photoanodes allowed infiltration of Co(II) ions across the entire film, enabling a large fraction of the internal surface area to be covered by the Co(II) cations which promote the photocatalytic water oxidation to oxygen under visible light. The obtained results provide us with a deeper understanding of the charge carrier reactions at the surface of the presently studied photoanode and open a path for understanding how to further improve its performance.

Results and Discussion

Materials characterisation of maghemite quantum dots.— Maghemite (γ-Fe_2O_3) nanoparticles (NPs) were obtained by hydrothermal synthesis using $FeCl_2.4H_2O$ as a precursor and a fixed amount of oleic acid to stabilize the colloid formed during hydrolysis. Polyethylene glycol (PEG) 20 000 was used as a surfactant. The synthesis was carried out in a Teflon vessel placed inside a Parr reactor for 3 h at 140 °C. The QDs were first characterised by high-

[z]E-mail: michael.graetzel@epfl.ch; ncv@fem.unicamp.br

resolution transmission electron microscopy (HR-TEM, Figs. 1a–1b). The nanoparticles are well distributed, and HR-TEM shows the lattice spacing of maghemite. Based on the histogram shown in Fig. 1c, their average size is calculated to be 3.3 nm ± 0.6 nm. Raman spectroscopy confirms the absence of contaminants or crystalline phases of other iron oxides. The spectral features shown in Fig. 1d are typical for the γ-Fe_2O_3 crystal with three peaks located at 365 cm^{-1}, 495 cm^{-1}, and 682 cm^{-1}.[29,30]

Morphology and chemical composition of the photoelectrodes.—The PEG-stabilised maghemite NPs were placed onto the conducting glass substrate (fluorine-doped tin oxide layer deposited on 1 mm thick aluminium-borosilicate glass) that exhibited a 10 ohm $square^{-1}$ sheet resistance. Films were annealed at 850 °C for 20 min to ensure better magnetic properties and photoresponse.[31–34] This process was repeated different times for the preparation of three kinds of samples with a different number of layers, namely, one layer (1L), two layers (2L), and three layers (3L). The morphology and thickness of different samples were characterised by surface and cross-sectional scanning electron micrographs and transmission electron micrographs (Figs. 2, S.1 in supporting information (available online at stacks.iop.org/JES/169/056522/mmedia)).

The average thickness of the three samples was obtained by measuring the cross-sectioned using a FIB technique (Fig. S1-see supporting information). The thickness values are 141 nm (± 28 nm) for 1-layer (1L), 158 nm (± 23.5 nm) for 2-layers (2L) and, 222 nm (± 20 nm) for 3-layers (3L). The morphology difference among three samples is also verified by SEM regarding the deposited layers, as shown in Figs. 2a–2c. One-layer sample conserves its globular sintering characteristics (Fig. S1.a). On top of the previously-sintered one, the second-layer deposition fill the gap of the first layer, resulting in only a slight increase of film thickness. Inspection of Figs. 1Sg–1Si shows that both the pore size and the pore wall thickness of the hematite film increase by adding the 2 additional layers. This is consistent with maintaining roughly the same porosity during this addition. This trend is maintained iupon adding one further particle layer to the film. This result is supported by observing only a slight increase of thickness when one more layer is added to the sample. Interestingly, the porosity of the studied material remains almost unchanged for 2L and 3L, regardless of the film thickness can be inferred from the cross-sectional images by SEM-STEM technique (Figs. 1Sg–1Si), and demonstrates the homogeneity of all samples along the *z*-axis. In addition, the sintering process under high temperature led to an indexed hematite phase (ICSD No. 7797) with strong preferential orientation along the [110] direction for hematite films, showing no other preferential orientation, as observed in Fig. 2f.

Figure 3a shows the XRD pattern of 1L, 2L, and 3L of hematite photoanodes identified as a corundum structure type with trigonal crystal phase. with a strong signal reflection of (110) and (104), both with hexagonal coordinates. The XRD peak (104) indicates sample texture created by high crystalline (self)-orientation at the same direction and high energy surface, leading the nanoparticles to assemble differently, such as (110) reflection.[21–23] The (104) peak of hematite and the (101) peak of SnO_2 lie close to each other, suggesting that the preferential growth at the interface film/substrate is mainly along [104] and then switches to [110] orientation. This affirmation agrees with TEM images in Fig. 2f, showing only (110) direction along with the hematite films. The same samples were evaluated by Raman spectroscopy (Fig. 3b). Seven hematite phonon modes predicted by group theory are identified by Raman analysis, in good agreement with previous studies.[35–38] The Raman spectrum

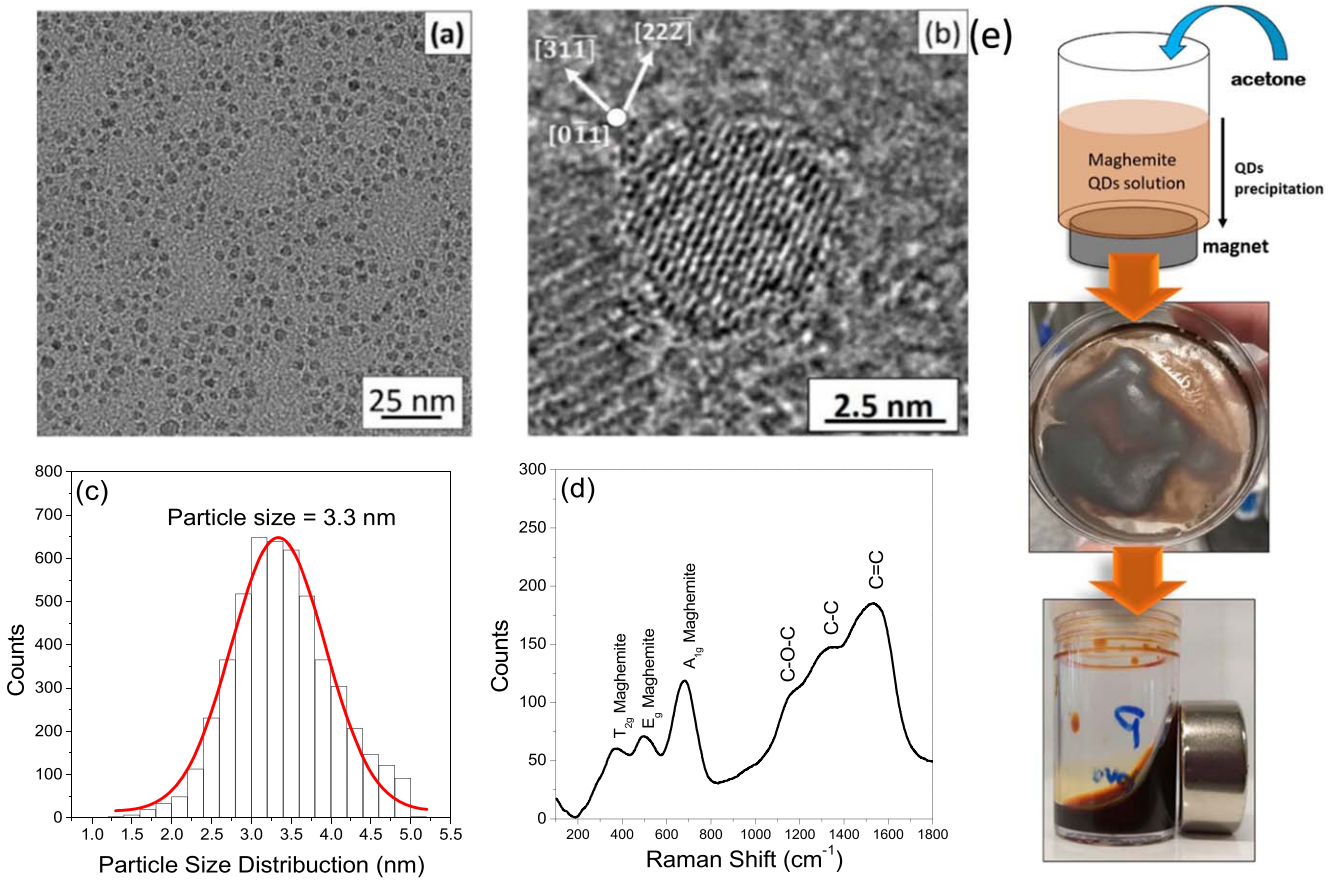

Figure 1. (a)–(b) HR-TEM images and (c) TEM histogram of particle size distribution of maghemite NPs, (d) Raman spectra of the maghemite powder following its synthesis and (e) schematic representation of the collection of maghemite NPs prepared by hydrothermal synthesis for film preparation and analysis.

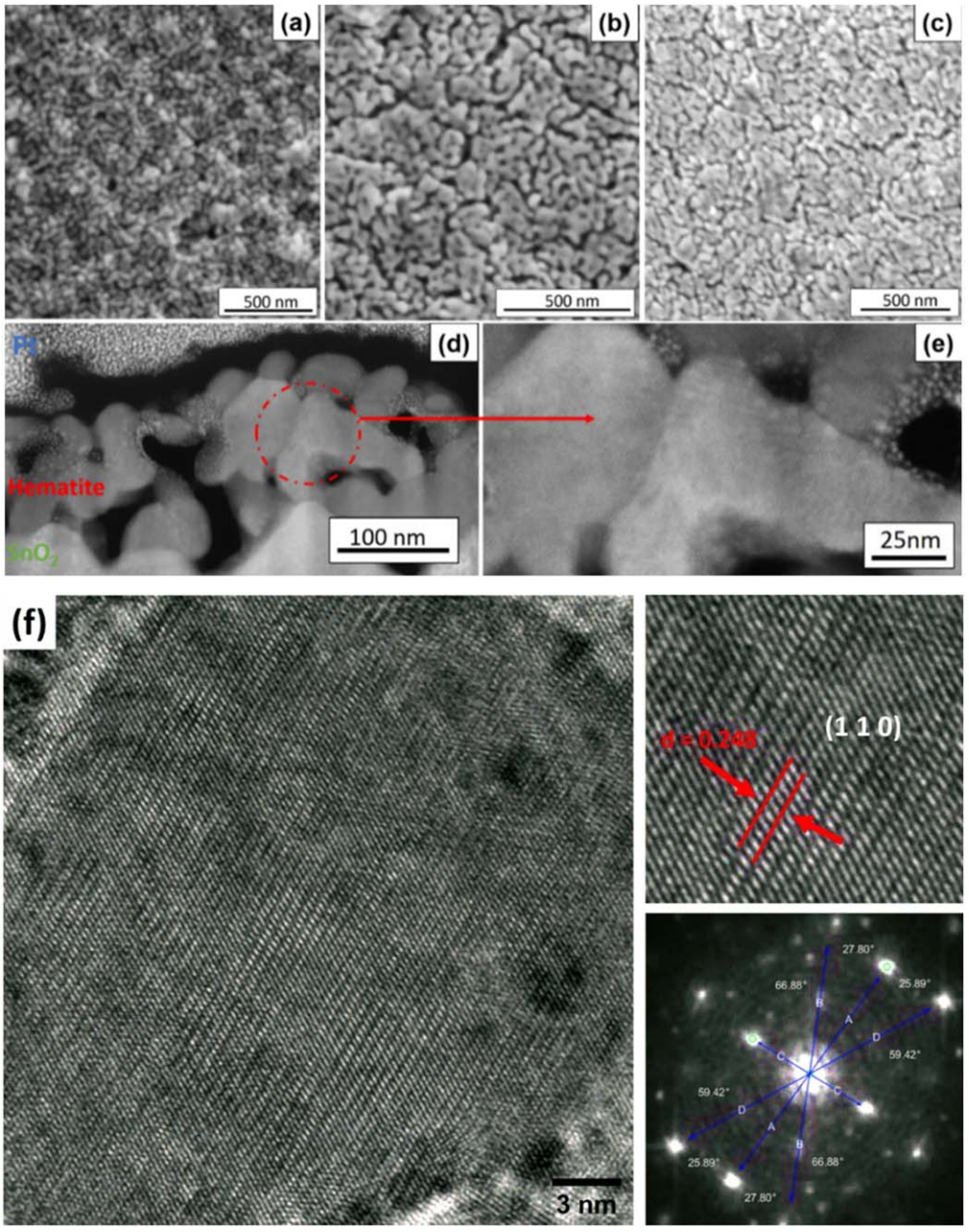

Figure 2. SEM top-view images (a)–(c) for 1L, 2L, and 3L, respectively and (d)–(e) STEM-SEM of a cross-section layer of the hematite film, with a view of its porous morphology after heat treatment, (f) high-resolution HAADF-STEM image of cross-sectional hematite layers with an FFT analysis of the hematite grain, showing preferential growth along the [110] orientation.

also confirms the purity of hematite excluding substantial levels of impurities such as formed by other iron oxides, crystalline phases, or SnO_2.

Additional images and EDS analysis were performed on the sample cross-sections in order to observe whether there was infusion of tin (IV) cations into the hematite grains caused by the high temperature (850 °C) during sintering process. Figure 3c corroborates the results from Figs. 3a–3b demonstrating a highly pure hematite film. While the atomic fraction of Sn present in the hematite is only 0.13, % this suffices to increase significantly the n-doping of the hematite particles. Diffuse reflectance spectroscopy (DRS) was also performed (see Fig. S2-Supporting Information) to determine the bandgap energy by intercepting the tangent of the Kubelka–Munk function plot for the hematite films. The bandgaps are 2.00 eV for the 1L sample, 2.05 eV for the 2L sample, and 1.95 eV for the 3L sample, which is consistent with the known bandgap of hematite, ranging from 1.95 to 2.1 eV.[5,39]

Photoelectrochemical performance for water oxidation.— Photoelectrochemical characterisation of 1L, 2L and 3L films was performed in a total of 9 samples of each composition, and a best fit curve was chosen to represent the data set as outlined in Fig. 4. Figure 4a shows the UV–vis absorption spectra. The absorbance starts to increase below 700 nm for 2L and 3L electrodes and strongly below 600–650 nm o for all electrodes, consistent with the 1.9–2.1 eV hematite bandgap. Figure 4b shows the photocurrent response of hematite samples with a negligible dark current due to a low catalytic current in the anodic region. In contrast, the measurements performed under simulated AM 1.5 G sunlight show photocurrent densities of 0.81 ± 0.04 mA cm^{-2} for 1L, 1.34 ± 0.06 mA cm^{-2} for 2L, and 1.80 ± 0.05 mA cm^{-2} for 3L at a

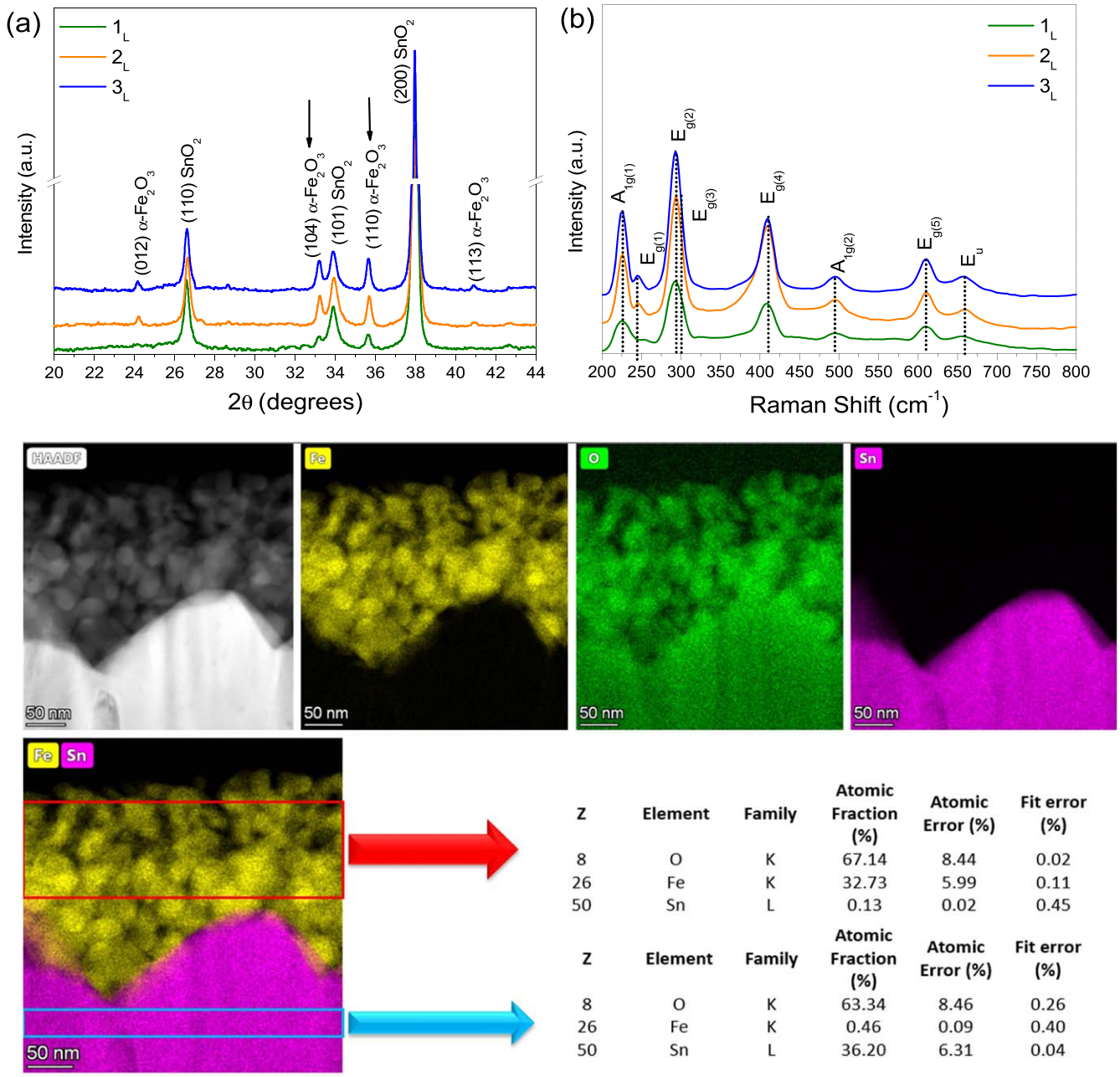

Z	Element	Family	Atomic Fraction (%)	Atomic Error (%)	Fit error (%)
8	O	K	67.14	8.44	0.02
26	Fe	K	32.73	5.99	0.11
50	Sn	L	0.13	0.02	0.45

Z	Element	Family	Atomic Fraction (%)	Atomic Error (%)	Fit error (%)
8	O	K	63.34	8.46	0.26
26	Fe	K	0.46	0.09	0.40
50	Sn	L	36.20	6.31	0.04

Figure 3. (a) XRD pattern and (b) Raman spectra of hematite surface films after heat treatment at 850 °C for 20 min. XRD signal and peak assignment for each phonon mode are observed for 1, 2, and 3-layers, and (c) TEM-EDS of cross-section samples to check the extend of Sn(IV) diffusion into hematite-layer.

potential of 1.23 V_{RHE}. However, adding a fourth layer (4L) decreases the photocurrent density at 1.23 V_{RHE} to 0.65 mA cm^{-2} (see Fig. S3-supplementary information).

The surface roughness factors of hematite electrodes were obtained by cyclic voltammetry. The obtained average values of five measurements were 27 for 1L, 59 for 2L, and 80 for 3L films, respectively (Fig. S4). These values correspond to the projected geometric surface area (0.196 cm^2 divided by the electrochemical surface roughness) given the active surface area (ECSA): 5.3 cm^2, 10.8 cm^2 and 15.8 cm^2 for the 1L, 2L and 3L films, respectively. The photocurrent response of different samples are mainly determined by the film thickness apart from the surface roughness and the orientation of the crystal planes (Figs. 2d–2f and 3a). Figure 4c shows current-voltage curves in the presence of H_2O_2 acting as a hole scavenger. This technique is suitable for measuring $P_{injection}$ in hematite photoanodes used for water splitting. It´s worth nothing to say that the photoelectrochemical experiments were conducted using an aqueous electrolyte solution prepared with 1 M NaOH + 0.5 M H_2O_2. The aim is to compare the difference of photocurrent obtained in with H_2O_2 as a scavenger (surface recombination suppressed) with a water-based electrolyte - without H_2O_2 to observe the extent of surface recombination. The method and thin-film calculation for $P_{injection}$ and $P_{charge\ separation}$ were performed using Dotan and co-authors.[40] The H_2O_2 is a good choice when it comes to hematite photoanode; once it does not corrode, hematite thin film is transparent to visible and ultraviolet light. The H_2O_2 has a rate constant for oxidation that is 10 to 100 times higher than that of water with a negative O_2/H_2O_2 couple ($E^0 = +0.68\ V_{RHE}-$) when compared with the O_2/H_2O couple ($E^0 = +1.23\ V_{RHE}$ for).[40]

Hole transfer efficiency at the interface.—The absorbed photocurrent density (J_{abs}) of the samples was quantitatively estimated

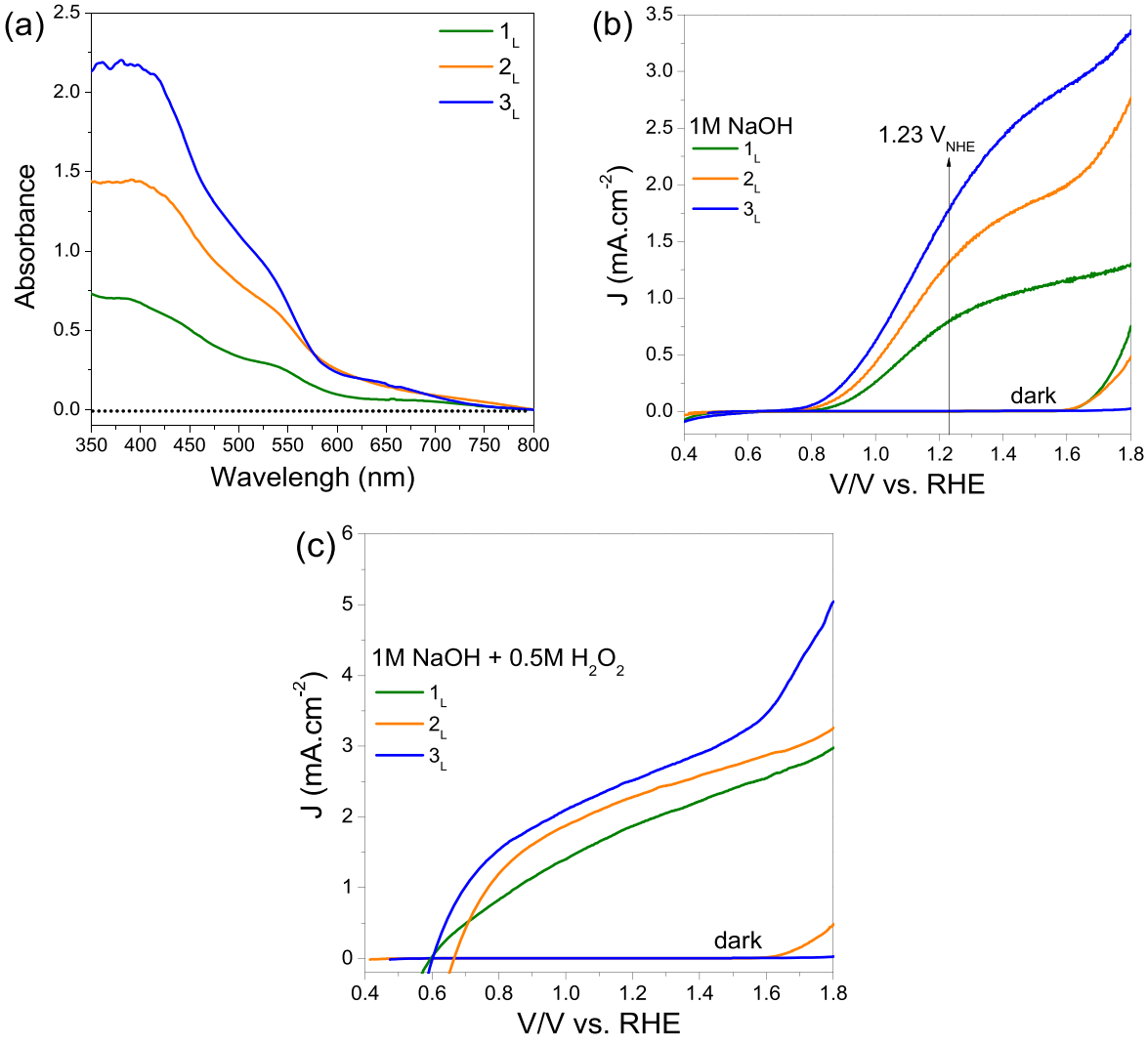

Figure 4. (a) UV–vis absorption spectra of the hematite photoanodes, (b) current potential (J vs E) curves of the sintered electrodes after heat treatment under front-side illumination and in dark conditions 1 M NaOH, (c) current potential (J vs E) curves in 1 M NaOH—0.5 M H_2O_2.

using the following equation:

$$J_{abs} = q \int_{300}^{800} f(\lambda).A(\lambda).d(\lambda).T \quad [1]$$

Where q is the electron charge, $F(\lambda)$ is the irradiance spectrum (mA cm^{-2} s^{-1} nm^{-1}) of the light source used for photoelectrochemical measurements (150 W Xe lamp (100 mW cm^{-2}) and $A(\lambda)$ is the absorptance spectrum obtained from the UV–vis spectra for the hematite film.

The absorbed photocurrent density (Fig. 5a) calculated for all layered hematite films depends on their thickness and represents the maximum theoretical current that could be achieved for the studied electrodes. For example, the 1L sample can reach a theoretical value of 8.5 mA cm^{-2}, while the calculation for 2L and 3L results in projected photocurrents up to 12.8 mA cm^{-2} and 14.5 mA cm^{-2}, respectively. We further determine the charge separation efficiency as well as the injection efficiency via the following equations:

$$P_{charge\ separation} = J_{H_2O_2}/J_{abs} \quad [2]$$

$$P_{injection} = J_{H_2O_2}/J_{H_2O} \quad [3]$$

J_{H2O} represents the photocurrent measured in 1 M NaOH water solution. J_{H2O2} is the photocurrent using H_2O_2 as a hole scavenger.

The trends for $P_{charge\ separation}$ and $P_{injection}$ on three samples are shown in Fig. 5b. 1L sample delivered efficiency of 22% at 1.23 V_{RHE}, while the efficiencies of the 2L sample and 3L samples are 20% and 17% at the same applied voltage, respectively. Thus, this demonstrates a lower charge separation rate for thicker films with the studied hematite photoanodes. The 3L sample showed the injection efficiency of 70% at 1.23 V_{RHE}, while the values of Pinjection for 1L and 2L samples are only 39% and 48% at the same potential, respectively. Thus, this demonstrates that 3L sample has the smallest percentage of holes that are loosed via recombination with electrons.[40,41]

Benefiting from the highest injection efficiency, the 3L sample showed the best performance of the three films tested. It generated a photocurrent of 3.3 mA cm^{-2} corresponding to a photocurrent generation efficiency of 22.7%. If our Fe_2O_3 photoanode would be coupled in a tandem cell with a photocathode that absorbs wavelength from the solar emission beyond 600 nm and delivers a cathodic photocurrent for hydrogen evolution of at least 3.3 mA cm^{-2} at 1.23 V_{RHE} the device would split water with a solar to hydrogen energy conversion efficiency of $3.3 \times 1.23 = 4\%$.

It is known that donor states in hematite are associated with oxygen vacancies (V_O) located below the conduction band and partly responsible for the intrinsic n-type conductivity observed.[22] Meanwhile, the electrical conductivity and band bending at the photoanode surface facilitated the separation of photoinduced charge

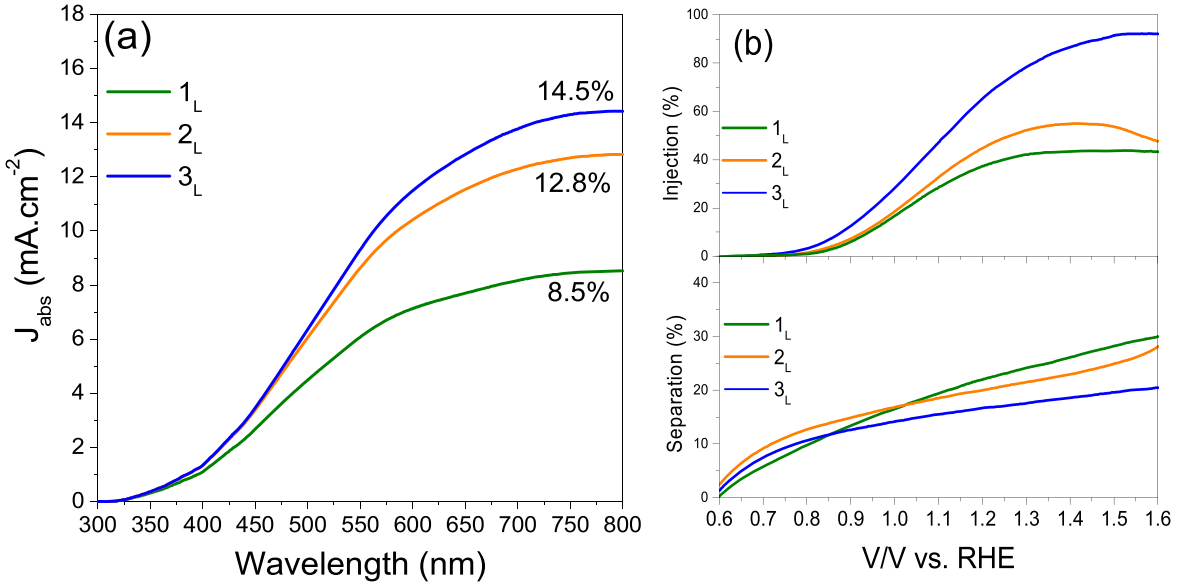

Figure 5. (a) J_{abs} values calculated from the absorptance of the films and integrating them with respect to the AM 1.5 G solar emission spectrum, (b) yield of charge separation and yield of charge injection in hematite electrodes.

carriers. Forster et al. employed the transient absorption spectroscopy technique to illustrate that the oxygen vacancy (V_O) can block the surface electron-hole recombination and improve electron collection.[42,43] During thermal treatment at 850 °C for each layer, it is known that two Fe^{2+} ions will form for each oxygen vacancy, creating mixed hematite valence.[44] Thus, it is noted that hematite is anti-ferromagnetic, and its unit cell consists of 30 atoms where Fe^{3+} is six coordinated and O^{2-} are four coordinated.[45] The Fe^{2+}/Fe^{3+} mixed valence states are present in the [110] axis (XRD diffractogram—Fig. 3a). The Fe^{3+} is associated with holing trapping by ferric acceptors, in which electrons are trapped at a Fe^{3+}–V_O complex forming a Fe^{2+}–V_O, while Fe^{4+} serves as a recombination site.[22,46] Because of this characteristic, the hexagonal coordinate shows a conductivity value of the [001] orientation by up to four orders of magnitude.[47] Thus, the [110] axis is likely to be the primary and most active facet for hematite water oxidation in our photoanodes.[48,49]

Enhancement of the oxygen evolution reaction (OER) on hematite by surface treatment with Co(II) ions.—In order to enhance the photoelectrochemical performance of bare-hematite photoanodes, we immersed the samples in an aqueous solution containing 1 mM $Co(NO_3)_2$ for 10 min, followed by rinsing with water to remove any Co(II) excess.[4] The cobalt treatment leads to the drop of the onset potential of the OER by 170, 120, and 110 mV for $1_{L\text{-}Co}$, $2_{L\text{-}Co}$, and $3_{L\text{-}Co}$, hematite films respectively. Figure 6a shows the comparison of the photocurrent response for the three types of films with values of: 0.9 ± 0.08 mA cm^{-2} for $1_{L\text{-}Co}$, 2.1 ± 0.03 mA cm^{-2} for $2_{L\text{-}Co}$ and 3.3 mA cm^{-2} ± 0.08 for $3_{L\text{-}Co}$ films.

We conclude that due to its porosity when the cobalt precursor is added to the samples, Co^{+2} ions managed to impregnate themselves to the pores near the base of the TCO. Surface roughness values were calculated by electrochemical method (Fig. S5—support information), indicating that the cobalt filled in the previously observed gaps/pores, leading to a significant increase in the obtained surface roughness values became more "detectable and active sites." The cobalt addition to bare samples leads to an increase of 1.8 times the photocurrent response (≅84%) for $3_{L\text{-}Co}$ in this studied system. The obtained results for samples with and without cobalt are compared in Table I.

The remarkable photocurrent density achieved on our hematite photoanode is due to its specific mesoscopic structure enabling deep

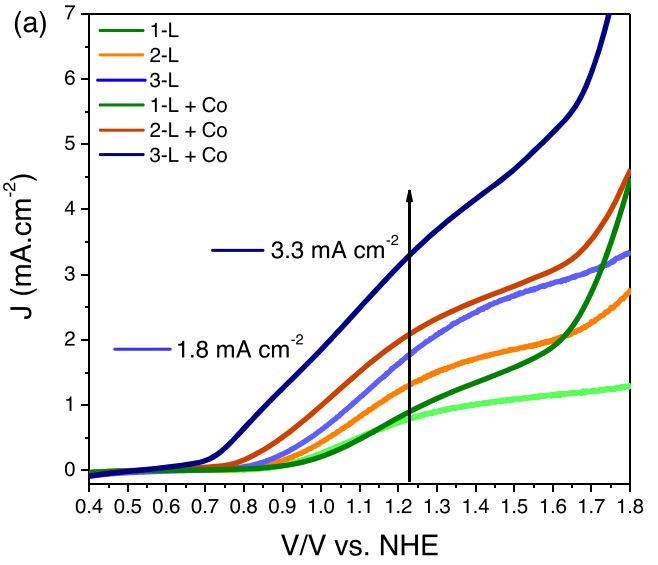

Figure 6. Comparative graphic of current potential (J vs E) curves of bare-hematite and hematite-Co under front-side illumination.

and complete infiltration of the film with Co(II) ions. In addition, the increased collection efficiency of photogenerated charge carriers may be to the hole storage effect exerted by the adsorbed Co(II) ions which reduces the rate of charge carrier recombination.[50–52] Our findings corroborate previous studies regarding the role of Co(II) ions adsorbed at the surface of hematite in promoting the overall transfer of holes to 2 water molecules to form molecular oxygen and 4 protons.[50–61]

The mechanism of the OER on hematite was already explored by Graetzel[4,62] and Durant groups,[48,63,64] who noted that the valence-band holes created by visible light illumination of hematite have mainly Fe^{IV}—character, resulting in a low-rate constant for water oxidation. Trapping of photo-generated holes on Fe(III) surface site leads to higher valent Fe^{IV}-oxo species ($> Fe^{IV} = O$) as the first intermediates of the OER.[46,48,60] At low surface concentration of $>Fe^{IV} = O$ the oxygen evolution proceeds on a single $>Fe^{IV} = O$ site via a $>Fe^{IV}$–O–OH peroxide intermediate and follows first order

Table I. Comparative table values of *J* values m onset potential and surface morphology determined from photoelectrochemical measurements.

Sample	Bare Hematite				Hematite +Co			
	J (mA cm^{-2})	Onset (mV)	RF	ECSA	J (mA cm^{-2})	Onset (mV)	RF	ECSA
1L	0.81	0.69	27.3	5.3	0.92	0.58	36.7	7.2
2L	1.34	0.69	59.5	10.8	2.10	0.52	83.8	16.4
3L	1.80	0.65	80.6	15.8	3.32	0.52	123.6	24.2

kinetics.[48] By contrast, at higher $>Fe^{IV} = O$ surface concentrations the OER proceeds via a m-oxo-dimer of $>Fe^{IV} = O$ and follows third order in $>Fe^{IV} = O$ concentration.

Figure 7 shows a possible pathway for the OER on the Co^{II}-modified hematite surface. holes may be trapped by Fe^{II}/Co^{II} sites as Fe^{III}/Co^{III}, which in turn can be further oxidised to Fe^{IV}/Co^{IV}.[4,22,50,53,65] Nucleophilic attack by water leads to oxygen release and regeneration of the form of a peroxo/oxo-intermediate, and while the role hole trapping occurs and storage by the surface adsorbed Co(II) reduces electron hole recombination sites allowing the accumulation of oxidation equivalents, leading to the desired shift in the onset of the photocurrent to lower voltage a better photoresponse for the studied materials.[4] Thus, in this work, it is essential to consider the sample's high porosity, and it is possible to conclude that the penetration of Co(II) ions can proceed into the deepest pores of hematite films for 1L, 2L and 3L, as schematically represented in Fig. 7.

Because of the high performance, of our bare hematite photoanode they offer ample room for further improvement as OER photocatalysts. In this work, cobalt was chosen as the co-catalyst to improve electrode efficiency. Our results corroborate previous works using cobalt as a catalyst on hematite photoanodes. Using a simple, environmental-friendly method and easy deposition, our photoanode was able to match with a single Co^{2+}-layer deposition the results reported by Tilley resorting to the expensive IrO_2 noble metal catalyst to promote solar water splitting to oxygen on hematite photoanodes.

Conclusions

This work presented a low-cost and environmentally friendly hydrothermal synthesis route to prepare hematite photoanodes with various thicknesses on TCO glass by drop-casting. Three-layer photoanode showed a photocurrent density of 1.8 mA cm^{-2} (bare-hematite) and 3.32 mA cm^{-2} (hematite-Co) for water oxidation at 1.23 V_{RHE} in 1 M NaOH. The film was highly-orientated along [110] and [104] directions, which improved the transport of charge carriers. A detailed analysis of the charge carrier behavior was performed. Adsorption of Co- improved greatly the photoanode performance and studying the interfacial charge transfer of those electrodes. We conclude that our work demonstrates that hydrothermal synthesis is a feasible method for fabricating highly efficient hematite photoanode by improving materials synthesis methods and achieving a new design for such nanostructured films with the aim to enhance hematite water oxidation performance.

Experimental Section/Methods

Synthesis of maghemite nanoparticles.—To obtain maghemite (γ-Fe_2O_3) quantum dots, 1.0 g of iron (II) chloride tetrahydrate ($FeCl_2.4H_2O$ - Aldrich Chemical 99.99%) was dissolved in 40.0 ml of mili-Q water together with 5 ml of a 25% PEG solution (polyethylene glycol 20000 -Aldrich Chemical) and 5.0 ml of oleic acid ($CH_3(CH_2)_7CH{=}CH(CH_2)_7COOH$—Aldrich Chemical $\geqslant$ 99.0%). After complete dissolution, 10.0 ml of ammonium hydroxide (NH_4OH, 28.0% NH_3 basis—Aldrich Chemical) were added under stirring. This solution was placed in a Teflon vessel into a Parr reactor and heated at 140 °C for 3 h with vigorous stirring. The maghemite quantum dots were separated via centrifugation and washed with mili-Q water. Acetone was added in a 1:4 ratio for particle decay, and a neodymium magnet was placed under the beaker with the solution to facilitate the separation of the nanoparticles. 0.5 M tetramethylammonium hydroxide pentahydrate aqueous solution ($(CH_3)_4N(OH).5H_2O$, $\geqslant$ 97%) - Aldrich Chemical) was used to stabilise the γ-Fe_2O_3 forming a stable colloidal solution.

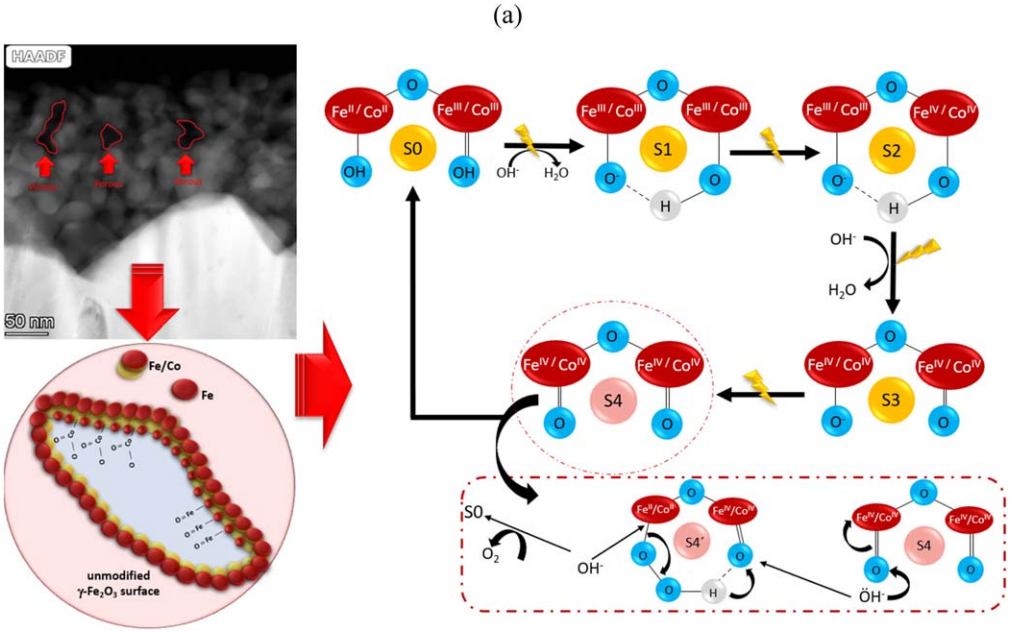

Figure 7. Schematic representation of (a) cobalt penetration onto porous hematite film and its oxo-groups mechanistic surface reaction under simulated sunlight.

Thin film deposition.—The TCO substrate (fluorine-doped SnO_2 coated on aluminoborosilicate glass from Solaronix S.A.) was washed with isopropanol and rinsed several times with pure water, followed by drying at room temperature in air. Thin films were deposited by dripping 10 μl of the colloidal solution on top of the substrate. A total of 9 electrodes of each composition were prepared, and then the samples were heat-treated at 850 °C for 20 min for each deposited layer to promote the maghemite/hematite phase transformation.

Characterisation.—A TEM Talos and Titan Themis at 300 kV with Cs correction was used for HR-TEM analysis, acquiring micrograph data of NPs from the dispersion of particles in toluene dripped on a carbon-coated copper grid. The mean average particle size was evaluated by ImageJ software based on 5000 measurements. The top-view film morphology was characterised by SEM (Quanta-FEG 650 - FEI) under a high vacuum and an acceleration voltage of 2.0–5.0 kV. The cross-sectional film characterisation was performed by Helios Nanolab (FEI- Dual-beam 660), and samples were obtained by FIB technique to produce samples for atomic resolution STEM imaging. X-ray diffraction experiments were carried out using a Bruker Advance D8 with Cu-Ka radiation (λ = 1.5418 **Å**) generated at 40 kV and 30 mA. Experiments scanned 2θ from 20° to 45° with 0.04° per step with multiple scans up to 2 h, generating an integrated graph of all scans at the end of analysis. Raman spectroscopy measurements were carried out on a Horiba Scientific, with 0.1% filter, at room temperature, with laser intensities in the range of 0.2–6.0 mW. Ultraviolet–visible (UV–vis) absorption of the samples was recorded on a MultiSpec-1501, Shimadzu UV–vis spectrophotometer equipped with an integrating sphere. Data was collected in a wavelength range of 300 nm to 800 nm. The diffuse reflectance spectroscopy (UV–vis/DRS) of the analysed samples was obtained by a Shimadzu-2600, coupled with an integrated sphere, in a wavelength range of 200 nm to 1100 nm.

Photoelectrochemical measurements.—The photoelectrochemical analysis was carried out in a standard three-electrode cell using an Ag/AgCl reference electrode and a platinum chain as a counter electrode (10 × 20 mm). The hematite film was used as the working electrode (0.196 cm^2) in a 1 M NaOH and 1 M NaOH + 0.5 M H_2O_2 solution. All potentials reported here are given against reversible hydrogen electrode (RHE). A potentiostat/galvanostat Autolab 320 N with an FRA-32M electrochemical impedance module was used to measure dark and photocurrents at a scan rate of 20 mV s^{-1}. The photocurrents measured under light were obtained using a 150 W Xe lamp (100 mW cm^{-2}), the UV and IR part being cut off using an AM 1.5 G solar radiation filter from Oriel, Newport.

Roughness factor.—The electrochemically active surface area (ECSA) and roughness factor of each hematite photoanode (1L, 2L, and 3L samples) were estimated by determining the double-layer capacitance of the interface via cyclic voltammetry. The analysis was performed in triplicate in 1 M NaOH solution with a pH value of 13.8, and no significant change in values was identified. The double-layer optimal region was estimated by its non-Faradaic region (0.1 V window near open circuit potential). A potentiostat/galvanostat, Biologic SP-200, was used to perform cyclic voltammetry experiments at a scan rate of 100, 200, 300, 400, and 500 mV s^{-1}. The surface roughness factor of the prepared photoanodes was evaluated by its electrochemical double-layer capacitances in a 1 M NaOH solution, in a range of 0.1 V to 0.3 V vs Ag/AgCl for B–H and −0.2 V to −0.1 V vs Ag/AgCl for H-Co photoanodes with different scan rates (100, 200, 300, 400, and 500 mV s^{-1}). The charging current (i_c) is assumed to be equal to the product of the electrochemical double-layer capacitance (C_{DL}) and the scan rate (υ) as shown in Eq. 7 below.[66–68]

$$\mathbf{i_c = .C_{DL}} \quad [7]$$

Plotting i_c as a function of υ yields produce a straight line, of which the slope is equal to C_{DL}. The electrochemically active surface area (ECSA) of the electrode can be calculated by dividing C_{DL} by the specific capacitance (C_s) of the sample as shown in Eq. 8:[66–69]

$$\mathbf{ECSA = C_{DL}/C_s} \quad [8]$$

Where the specific capacitance (C_s) is 0.040 mF cm^{-2} for 1 M NaOH,[67] the roughness factor can be calculated by dividing the active surface area by the electrode area (0.196 cm^2).

Acknowledgments

The authors acknowledge the financial support provided by FAPESP (São Paulo Research Foundation, Brazil: grant 2018/13243-2 and 2019/26005-5), and the Swiss National Science Foundation (grant No. 514259). In addition, the authors would like to thank the Brazilian Nanotechnology National Laboratory (CNPEM-LNNano) and the Laboratory of Photonics and Interfaces (LPI) at EPFL for providing access to their facilities to perform the characterisation techniques used in this study.

ORCID

N. C. Verissimo https://orcid.org/0000-0002-2399-2140
D. Ren https://orcid.org/0000-0003-3738-6421
C. C. C. Kleiner https://orcid.org/0000-0002-1947-1887
F. A. B. Hesse https://orcid.org/0000-0002-1756-9338
S. M. Zakeeruddin https://orcid.org/0000-0003-0655-4744
M. Grätzel https://orcid.org/0000-0002-0068-0195
R. Bertazzoli https://orcid.org/0000-0002-2732-2312

References

1. S. Shen, S. A. Lindley, X. Chen, and J. Z. Zhang, *Energy Environ. Sci.*, **9**, 2744 (2016).
2. K. Sivula, F. Le Formal, and M. Grätzel, *ChemSusChem*, **4**, 432 (2011).
3. J. Y. Kim, G. Magesh, D. H. Youn, J.-W. Jang, J. Kubota, K. Domen, and J. S. Lee, *Sci Rep.*, **3**, 1 (2013).
4. A. Kay, I. Cesar, and M. Grätzel, *J. Am. Chem. Soc.*, **128**, 15714 (2006).
5. V. A. N. Carvalho, R. A. S. Luz, B. H. Lima, F. N. Crespilho, E. R. Leite, and F. L. Souza, *J. Power Sources*, **205**, 525 (2012).
6. R. H. Gonçalves and E. R. Leite, *Energy Environ. Sci.*, **7**, 2250 (2014).
7. W. M. Carvalho Jr and F. L. Souza, *Sol. Energy Mater. Sol. Cells*, **144**, 395 (2016).
8. S. C. Warren, K. Voïtchovsky, H. Dotan, C. M. Leroy, M. Cornuz, F. Stellacci, C. Hébert, A. Rothschild, and M. Grätzel, *Nat. Mater.*, **12**, 842 (2013).
9. N. J. Cherepy, D. B. Liston, J. A. Lovejoy, and H. Deng, *J. Phys. Chem. B 1998*, **102**, 770 (1998).
10. E. Thimsen, F. Le Formal, M. Grätzel, and S. C. Warren, *Nano Lett.*, **11**, 35 (2011).
11. J. Liu, Y. Y. Caia, Z. F. Tian, G. S. Ruan, Y. X. Ye, C. H. Liang, and G. S. Shao, *Nano Energy*, **9**, 282 (2014).
12. S. P. Schwaminger, R. Surya, S. Filser, A. Wimmer, F. Weigl, P. Fraga-García, and S. Berensmeier, *Sci Rep.*, **7**, 1 (2017).
13. P. S. Shinde, A. Annamalai, J. H. Kim, S. H. Choi, J. S. Lee, and J. S. Jang, *Data Br.*, **5**, 796 (2015).
14. I. Cesar, A. Kay, J. A. G. Martinez, and M. Grätzel, *J. Am. Chem. Soc.*, **128**, 4582 (2006).
15. D. Liu, Z. Li, W. Wang, and G. Wang, *J. Alloys Compd.*, **654**, 491 (2016).
16. W. M. Carvalho and F. L. Souza, *ChemPhysChem*, 2710 (2016).
17. Y. J. Chen and L. Y. Chen, *Energy Procedia*, **61**, 2046 (2014).
18. K. G. Upul Wijayantha, S. Saremi-Yarahmadi, and L. M. Peter, *Phys. Chem. Chem. Phys.*, **13**, 5264 (2011).
19. S. Kment et al., *ACS Nano*, **9**, 7113 (2015).
20. M. Barroso, S. R. Pendlebury, A. J. Cowan, and J. R. Durrant, *Chem. Sci.*, **4**, 2724 (2013).
21. R. Schrebler, L. A. Ballesteros, H. Gomez, P. Grez, R. Cordova, E. Muñoz, R. Schrebler, J. R. Ramos-Barrado, and E. A. Dalchiele, *J. Electrochem. Soc.*, **161**, H903 (2014).
22. Gurudayal et al., *ChemSusChem*, **10**, 2449 (2017).
23. M. Li et al., *Nano Lett.*, **17**, 2490 (2017).
24. Y. Hou, C. Zheng, Z. Zhu, and X. Wang, *Nanoscale Res. Lett.*, **41**, 20001 (2020).
25. Y. Hou, C. Zheng, Z. Zhu, and X. Wang, *Chem. Commun.*, **52**, 6888 (2016).
26. Z. Chen, L. Li, C. Liu, Y. Qiu, and N. Mitsuzak, *J. Alloys Compd.*, **696**, 980 (2017).

27. M. Y. Nassar, I. S. Ahmed, T. Y. Mohamed, and M. Khatab, *RSC Adv.*, **6**, 20001 (2016).
28. Y. Liu, F. Le Formal, F. Boudoire, and N. Guijarro, *ACS Appl. Energy Mater.*, **2**, 6825 (2019).
29. D. L. A. Faria, S. V. Silva, and M. T. Oliveira, *J. Raman Spectrosc.*, **28**, 873 (1997).
30. A. M. Jubb and H. C. Allen, *ACS Appl. Mater. Interfaces*, **2**, 2804 (2010).
31. G. B. Silva, M. Marciello, M. P. Morales, C. J. Serna, M. D. Vargas, C. M. Ronconi, and R. Costo, *J. Braz. Chem. Soc.*, **28**, 731 (2017).
32. S. M. Devi, A. Nivetha, and I. Prabha, *J. Supercond. Nov. Magn.*, **32**, 127 (2019).
33. R. H. Gonçalves, B. H. R. Lima, and E. R. Leite, *J. Am. Chem. Soc.*, **133**, 6012 (2011).
34. R. L. Blake and R. E. HessevicK, *Am. Mineral.*, **51**, 123 (1966).
35. S.-H. H. Shim and T. S. Duffy, *Am. Mineral.*, **87**, 318 (2015).
36. D. L. A. Faria and F. N. Lopes, *Vib. Spectrosc.*, **45**, 117 (2007).
37. M. J. Massey, U. Baier, and R. Merlin, *Phys. Rev. B*, **41** (1990).
38. T. P. Martin, R. Merlin, D. R. Huffman, and M. Cardona, *Solid State Commun.*, **22**, 565 (1977).
39. L. A. Marusak, R. Messier, and W. B. White, *J. Phys. Chem. Solids*, **41**, 981 (1980).
40. H. Dotan, K. Sivula, M. Grätzel, A. Rothschild, and S. C. Warren, *Energy Environ. Sci.*, **4**, 958 (2011).
41. L. Xi, S. Y. Chiam, W. F. Mak, P. D. Tran, J. Barber, S. C. J. Loo, and L. H. Wong, *Chem. Sci.*, **4**, 164 (2013).
42. M. Forster, R. J. Potter, Y. Ling, Y. Yang, D. R. Klug, Y. Lid, and A. J. Cowan, *Chem. Sci.*, **6**, 4009 (2015).
43. J. Moir, N. Soheilnia, K. Liao, Pl O'Brien, Y. Tian, K. S. Burch, and G. A. Ozin, *ChemSusChem*, **8**, 1557 (2015).
44. Y. Ling, G. Wang, J. Reddy, C. Wang, J. Z. Zhang, and Y. Li, *Angew. Chemie - Int. Ed.*, **51**, 4074 (2012).
45. T. J. Smart and Y. Ping, *J. Phys. Condens. Matter*, **29**, 394006 (2017).
46. W. Clark and P. Broadhead, *J. Phys. C: Solid State Phys.*, **3**, 1047 (1970).
47. N. Iordanova, M. Dupuis, and K. M. Rosso, *J. Chem. Phys.*, **122**, 144305 (2005).
48. C. A. Mesa, L. Francàs, and K. R. Yang et al., *At. Chem.*, **12**, 82 (2020).
49. M. Cornuz, M. Grätzel, and K. Sivula, *Chem. Vap. Depos.*, **16**, 291 (2010).
50. M. Barroso, C. A. Mesa, S. R. Pendlebury, A. J. Cowan, T. Hisatomi, K. Sivula, M. Grätzel, D. R. Kluga, and J. R. Durrant, *Proc. Natl. Acad. Sci. U. S. A.*, **109**, 15640 (2012).
51. M. Barroso, A. J. Cowan, S. R. Pendlebury, M. Grätzel, D. R. Klug, and J. R. Durrant, *J. Am. Chem. Soc.*, **133**, 14868 (2011).
52. A. J. Cowan and J. R. Durrant, *Chem. Soc. Rev.*, **42**, 2281 (2013).
53. K. Shimizu, A. Lasia, and J. F. Boily, *Langmuir*, **28**, 7914 (2012).
54. A. Y. Ahmed, M. G. Ahmed, and T. A. Kandiel, *Appl. Catal. B Environ.*, **236**, 117 (2018).
55. T. P. Trainor, A. M. Chaka, P. J. Eng, M. Newville, G. A. Waychunas, J. G. Catalano, and G. E. Brown Jr, *Surf. Sci.*, **573**, 204 (2004).
56. H. H. Pham, M. J. Cheng, H. Frei, and L. W. Wang, *ACS Catal.*, **6**, 5610 (2016).
57. R. Peat and L. M. Peter, *J. Electroanal. Chem.*, **228**, 351 (1987).
58. T. A. Kandiel, *J. Photochem. Photobiol. A Chem.*, **403**, 112825 (2020).
59. F. Le Formal, N. Tétreault, M. Cornuz, T. Moehl, M. Grätzel, and K. Sivula, *Chem. Sci.*, **2**, 737 (2011).
60. B. Klahr, S. Gimenez, F. Fabregat-Santiago, T. Hamann, and J. Bisquert, *J. Am. Chem. Soc.*, **134**, 4294 (2012).
61. F. Le Formal, S. R. Pendlebury, M. Cornuz, S. D. Tilley, M. Grätzel, and J. R. Durrant, *J. Am. Chem. Soc.*, **136**, 2564 (2014).
62. S. D. Tilley, M. Cornuz, K. Sivula, and M. Grätzel, *Angew. Chemie - Int. Ed.*, **49**, 6405 (2010).
63. E. Pastor, J.-S. Park, L. Steier, S. Kim, M. Grätzel, J. R. Durrant, A. Walsh, and A. A. Bakulin, *Nat. Commun.*, **10**, 1 (2019).
64. C. A. Mesa, L. Steier, B. Moss, L. Francàs, J. E. Thorne, M. Grätzel, and J. R. Durrant, *J. Phys. Chem. Lett.*, **11**, 7285 (2020).
65. T. Lopes, L. Andrade, F. Le Formal, M. Grätzel, K. Sivula, and A. Mendes, *Phys. Chem. Chem. Phys.*, **16**, 16515 (2014).
66. S. Arumugam, Y. Toku, and Y. Ju, *Sci Rep.*, **10**, 1 (2020).
67. C. C. L. McCrory, S. Jung, I. M. Ferrer, S. M. Chatman, J. C. Peters, and T. F. Jaramillo, *J. Am. Chem. Soc.*, **137**, 4347 (2015).
68. K. Shimizu and J. F. Boily, *Langmuir*, **30**, 9591 (2014).
69. O. Ibukun and H. K. Jeong, *New Phys. Sae Mulli*, **69**, 154 (2019).